ACS APPLIED NANO MATERIALS

www.acsanm.org

Article

Nanocomposites of Titania/Reduced Graphene Oxide: Flexible Humidity Sensors Tuned via Photocatalytic Reduction

Sophia C. Bittinger,* Jana Struck, Finn Dobschall, Sophie Benthien, Hauke Hartmann, Hendrik Schlicke, Mona Kohantorabi, Heshmat Noei, and Tobias Vossmeyer*

Cite This: *ACS Appl. Nano Mater.* 2025, 8, 7428−7439

Read Online

ACCESS | Metrics & More | Article Recommendations | Supporting Information

ABSTRACT: In this study, we demonstrate the tunability of hybrid graphene oxide/reduced graphene oxide/titania nanocrystal (GO/rGO/TNC) films for resistive humidity sensing through photocatalytic reduction. Using a layer-by-layer spin-coating (LbL-SC) technique, we fabricate GO/TNC nanofilms with titania nanorods (TNRs) or nanoplates (TNPs) on various substrates, achieving high uniformity and precise control over the film thickness (15−150 nm). We investigate the evolution of the electrical, optical, and structural properties of these films, modulated by the photocatalytic activity of TNCs under UV exposure (254 nm) while varying the illumination time, TNC type, and film thickness. The inclusion of TNCs enhances the films' conductivity by several orders of magnitude compared to pure GO films under UV illumination and enables precise adjustment of the GO/rGO and (GO/rGO)/TNC ratios. This approach is used for tuning the sensitivity, response time, and response polarity of (GO/rGO)/TNC resistors on flexible substrates to changes in relative humidity (RH). TNP-based films demonstrate superior performance, achieving sensitivities of up to 2.2 and response times as short as 1 s over a broad range of RH levels (~35 to 85% and ~1 to 80%). Depending on the composition and RH level, the sensors exhibit both positive and negative resistive responses to increasing humidity. Gravimetric analyses show that films with varying GO/rGO ratios exhibit the same change in water mass uptake, indicating that the differences in resistive behavior are driven by UV-induced alterations in their chemical and electrical properties. Finally, we propose the use of these sensors to detect body-related humidity fluctuations, demonstrating their suitability for wearable electronics. Our results highlight the potential applicability of (GO/rGO)/TNC nanocomposites as highly customizable humidity sensors.

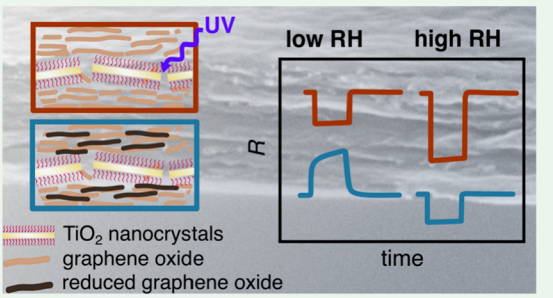

KEYWORDS: *graphene oxide, titania nanoparticles, composite, thin film, humidity sensor, photocatalysis, flexible sensor, chemiresistor*

INTRODUCTION

Flexible relative humidity (RH) sensors received considerable attention due to their applications in wearable electronics, particularly in healthcare, including respiration monitoring, speech recognition, and skin moisture measurements.[1,2] These sensors are operated based on various principles, such as capacitive, optical, bulk and surface piezoelectric, and resistive signal transduction.[3] Among these, resistive sensors are particularly attractive due to their straightforward readout procedure and ease of integration into electronic circuits. Depending on the target application, sensors must reliably measure very low humidity levels or perform effectively under high-humidity conditions, such as during respiration monitoring. However, traditional humidity sensors based on conductive polymers, ceramics, or metal oxides often have significant limitations, including nonlinear response isotherms, slow response and recovery times, low sensitivity, and high hysteresis, critical drawbacks for ensuring accurate, real-time humidity sensing in portable or wearable devices. To overcome these challenges, novel materials have been proposed for advanced humidity sensing, such as supramolecular nanoassemblies,[4] organic−inorganic polymer/metal nanoparticle hybrids,[5,6] 2D materials, e.g., MoS_2-based nanocomposites,[7] MXenes,[8] or carbon-based materials such as graphene oxide (GO), or reduced GO (rGO).[9]

GO-based nanomaterials are highly promising for humidity detection due to their exceptional hydrophilicity, large surface area, and flexibility. The GO surface is rich in polar functional groups that serve as sorption sites for water molecules. However, the sp^3 hybridization of lattice atoms gives GO an insulating character, limiting its use as a resistive sensor. Reduction methods can restore the sp^2 carbon system, producing rGO with enhanced conductivity but reduced humidity sensitivity due to the loss of oxygen-containing functional groups. Numerous studies have explored rGO-based

Received: November 20, 2024
Revised: February 24, 2025
Accepted: February 27, 2025
Published: April 7, 2025

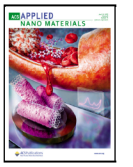

https://doi.org/10.1021/acsanm.4c06524
ACS Appl. Nano Mater. 2025, 8, 7428−7439

materials for resistive humidity sensing, focusing on reconciling these counteracting effects to optimize sensor performance.[10] Recently, Samorì and colleagues demonstrated that chemically introducing hydrophilic motifs onto rGO sheets significantly improves its sensitivity to humidity compared to pristine rGO resistors.[11] Furthermore, the combination of rGO with other nanomaterials can lead to synergistic effects and enhanced humidity sensing characteristics. For instance, recent works proposed hybrid layered films of rGO/silk fibroin,[12−14] rGO/polymer layers,[15,16] or rGO/Fe_2O_3 nanoparticle films,[17] among numerous others, as flexible, resistive sensors for the potential detection of physiological humidity.

Regarding the large number of studies, the reported resistive responses of GO/rGO-based materials to humidity vary from n-type to p-type, including mixed responses with conversions from n- to p-type behavior.[18−21] The observed responses often depend on the specific composition and structure of the material. rGO commonly exhibits p-type responses. This is due to disruptions in hole transport caused by interactions with water acting as an electron donor. In contrast, the more insulating GO typically shows n-type behavior, as water molecules induce ionic conductivity. In most studies, rGO was obtained from GO via thermal treatment or chemical reduction. In this regard, the combination of GO with TiO_2 nanocrystals (TNCs) offers numerous advantages: First, carboxylic acids (which are prominently present in GO) are known to strongly bind to TiO_2 surfaces, enabling the efficient fabrication of robust composites.[22] Second, TNCs are photocatalytically active and can provide photogenerated electrons for the reduction of GO upon UV irradiation. The photocatalytic reduction of GO was first reported in 2008 by Williams et al. for a GO/TiO_2 suspension in ethanol as a hole scavenger.[23] This method was further applied to composite thin films of GO/TiO_2, enabling the photocatalytic patterning of rGO films.[24−27] Additionally, in contrast to thermal or chemical reduction methods, photocatalytic reduction allows control over the degree of reduction by simply adjusting the illumination time. It also enables the selective removal of functional groups,[28] which is particularly advantageous for tuning the material's affinity toward polar analytes. Last, the incorporation of TNCs provides additional sorption sites for water molecules. Consequently, the photocatalytic reduction using TNCs is well suited to develop hybrid GO-based resistive sensors with both optimized electrical and sensing properties. For example, Lee et al. illuminated suspensions of GO and spherical TNCs in ethanol with UV light to photocatalytically reduce GO, and drop-casted the obtained composites onto electrode structures. They compared the resistive responses of the UV-treated and nontreated material toward reducing gases and reported switching from n- to p-type behavior after the formation of rGO within the composite.[29]

Here, we present a comprehensive study of (GO/rGO)/TNC hybrid nanofilms and their tunability via photocatalytic reduction for resistive humidity sensing. First, we present a layer-by-layer spin-coating (LbL-SC) method for the fast and efficient fabrication of uniform thin films comprising GO and titania nanorods (TNRs) or nanoplates (TNPs) on various substrates with adjustable composition and thickness. Then, we investigate the tunability of the electrical, optical, and structural properties of these hybrid films via the photocatalytic reduction of GO, by systematically varying the UV exposure time, TNC shape, size, concentration, and film thickness. The evolution of the films' composition is analyzed by charge transport measurements, scanning electron microscopy (SEM), and X-ray photoelectron spectroscopy (XPS). Furthermore, we demonstrate the use of the method to fabricate photocatalytically patterned films and highlight their application as resistive humidity sensors with widely tunable response characteristics.

EXPERIMENTAL SECTION

TNC Synthesis. TNRs and TNPs were synthesized following the Gordon method[30] as described in our previous work,[22] with slight modifications. Briefly, TNCs were obtained in a seeded-growth method at high temperatures. TNRs were obtained using $TiCl_4$ as a precursor, and TNPs using TiF_4. To obtain both TNC shapes, OLAM and OLAC were used as surfactants. Details of the synthesis process are provided in the Supporting Information, Section S2.

GO Synthesis. GO was synthesized following a modified Hummers method by Chen et al.[31] The experimental details are provided in the Supporting Information, Section S3.

Fabrication of Electrode Structures on Polyimide. A layer of gold (thickness: 50 nm) was deposited onto polyimide (PI) via thermal evaporation. The substrates were then coated with the negative-tone photoresist AZ nLOF 2020 via spin-coating (3000 rpm, 60 s, Suss MicroTec LabSpin 6 TT), and soft-baked for 60 s at 110 °C. Next, the resist-coated PI substrates were exposed through a photomask for 12 s by using a mask aligner (Karl Suss MJB-3). A postexposure bake was conducted for 60 s at 110 °C. The photoresist was developed for 60 s by immersion in the AZ 726 MIF developer, rinsed with DI water, and dried in a stream of nitrogen. Then, the exposed gold areas were removed by immersion in a gold etchant solution ($KI/I_2/H_2O$, 4/1/400, *m*/*m*/*m*) for approximately 2 min. The substrates were rinsed with DI water. The photoresist was removed by immersion in TechniStrip NI155 for 30 min at 65 °C, yielding the gold interdigitated electrode structures (IDEs) on PI (16 fingers, 125 μm width, distance: 125 μm, overlap of 4875 μm). The substrates were cleaned in the final step by subsequent immersion in acetone, 2-propanol, water, and then dried in a gentle stream of nitrogen.

Hybrid Film Fabrication. Materials and chemicals used in this study are TNCs/chloroform (0.5−4 mg/mL) and GO/water/methanol (~0.1 wt %, 1/3 v/v); methanol (99.8% VWR Chemicals) and DI water (purified with an ELGA LabWater purification system); Quartz slides (Won Ik Quartz Europe, 20 × 20 × 0.5 mm^3), PI (RS, Kapton ~20 × 10 × 0.05 mm^3), and SiO_2/Si wafers (<100> orientation, 500 nm SiO_2, diameter: 200 mm, thickness: 725 ± 10 μm, 8−25 Ω cm, p-doped, Si-Mat); and Si wafers (<100> orientation, diameter: 76.2 mm, thickness: 380 ± 20 μm, 8−25 Ω cm, Si-Mat) and QCMs (resonant frequency: 10.00 MHz, diameter: 14 mm, Ti/Au electrodes, QuartzPro).

Preparation of Substrates. Before film deposition, the desired substrates were treated in an air plasma (Harrick Plasma PDC-002) for 2 min, yielding hydrophilic surfaces.

GO/TNC Film Deposition. The desired substrate was placed on a spin-coater (Suss MicroTec LabSpin 6 TT) and constantly rotated at 3000 rpm. First, 25 μL of a methanolic/aqueous GO solution was applied to the rotating substrate. After 30 s, the deposition step was repeated. After 30 s, 25 μL of the desired TNC/chloroform solution was deposited onto the rotating substrate, followed by the deposition of 2 × 25 μL of GO solution, again each deposition step spaced by a 30 s delay time. This sequence was repeated 3−10 times, depending on the desired film thickness. For film deposition on QCMs, the substrates were placed slightly off-center on the spin-coater to avoid accumulation of the material in the central active area of the sensor. The QCMs were coated on one side.

Photocatalytic Reduction and Patterning of (GO/rGO)/TNC Films. Substrate-supported GO/TNC films were illuminated in ambient conditions with deep UV (DUV) light using a custom-built source (main emission at 254 nm; irradiance 520 mW/cm^2). Illumination times were varied from 15 min to 7 h. To prevent

https://doi.org/10.1021/acsanm.4c06524
ACS Appl. Nano Mater. 2025, 8, 7428−7439

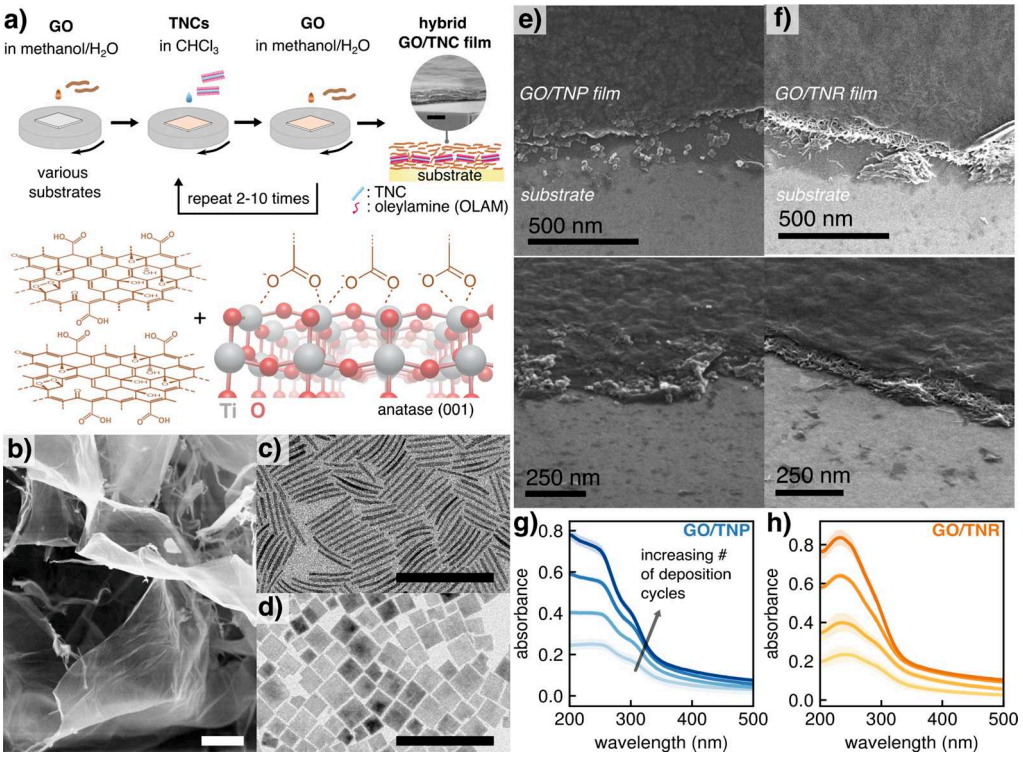

Figure 1. (a) Layer-by-layer spin-coating (LbL-SC) procedure to fabricate hybrid films by the alternating deposition of GO and TNCs on various substrates. The inset shows an SEM image of a multilayered GO/TNR film fabricated by applying 10 LbL-SC deposition cycles (scale bar: 200 nm). Schematic of the GO chemical structure and titania crystal surface with high affinities for carboxylic acid groups. (b) SEM image of freeze-dried GO (scale bar: 2 μm). (c, d) Exemplary TEM images of TNRs and TNPs used for film fabrication, respectively (scale bars: 100 nm). (e) SEM images of the edges of scratched GO/TNP and (f) GO/TNR films (four LbL-SC deposition cycles), respectively, deposited on a silicon wafer. (g, h) Absorbance spectra of hybrid films deposited on quartz substrates by applying 1−4 deposition cycles, fabricated using 2 mg/mL TNP- (blue) and TNR-solutions (orange), respectively. The shaded areas represent the standard deviations from the spectra measured at four different positions of the film.

overheating of the samples the setup was continuously ventilated using fans. For photocatalytic patterning, the films were illuminated through custom-designed quartz masks. To pattern well-defined microstructures, the samples were illuminated through a quartz mask using a Mask Aligner (Karl Suss MJB-3) equipped with a UV lamp (Osram HBO 200 W/DC, Hg lamp, multiline spectrum).

AFM analysis. The film thickness of GO/TNC and (GO/rGO)/TNC films deposited on oxidized silicon wafers was determined via AFM analysis using a digital instruments microscope equipped with a nanoscope IV controller. ∼1 × 1 cm^2 sections of the substrate-supported films were fixated on a metallic plate using sticky tape. The film was scratched several times using a cannula and subsequently cleaned in a stream of nitrogen to remove residues caused by scratching. Height maps (20 × 5 or 2.5 μm^2) were recorded at the edge of a scratched film and the underlying substrate at two different film positions using the tapping mode.

SEM Analysis. The film morphology before and after DUV exposure was analyzed via SEM analysis. GO/TNC films were deposited onto silicon wafers and exposed to DUV light for 7 h. The measurements were conducted using a Zeiss LEO 155 Gemini microscope (acceleration voltage: 30 kV).

Charge Transport Measurements. GO/TNC films were deposited on oxidized Si wafers equipped with IDE structures and exposed to DUV light for varying times. The samples were placed in a custom-built PTFE test cell (volume of ∼20 mL) and purged with nitrogen (Linde 5.0) for at least ∼1 min to remove adsorbed water molecules. The samples were contacted using spring-loaded pin connectors. Current−voltage curves were measured by using a Keithley 2601A sourcemeter or an Agilent 4165C semiconductor parameter analyzer. Voltages swept between ±1 and 0 V were applied (in 0.02 V steps), and the resulting current was recorded.

XPS Measurements. Hybrid films with incorporated TNRs and TNPs (2 mg/mL in chloroform) were deposited on Ti/Au-coated silicon wafers (2 × 2) cm^2, Ti/Au thickness: 10 nm/100 nm) by LbL-SC (one deposition cycle). After the deposition, the substrate was divided into four equal sections. The different sections were exposed to DUV light for 30 and 240 min for GO reduction. One section was left untreated as a reference. Measurements were made using a high-resolution two-dimensional delay line detector. Incident radiation was provided by a monochromatic Al K_α X-ray source (photon energy 1486.6 eV; anode operating at 15 kV). Spectra were acquired in a fixed transmission mode. A pass energy of 25 eV was chosen, resulting in a resolution of <0.4 eV. A flood gun was used during the measurements at an energy of 2.0 eV with 20 μA emission to compensate the charging effect. The binding energies were calibrated using the C 1s peak at 284.8 eV.

Resistive Humidity Sensing. Resistive responses of (GO/rGO)/TNC films on PI substrates to changes in the RH at ambient temperature were investigated. Hybrid films deposited on substrates equipped with 2 IDEs were exposed to DUV light through a quartz mask for 30−120 min. After DUV exposure, the PI substrate was cut to obtain two separate sensors that were placed in a test cell (PTFE, volume: 20 mL).

The setup was adapted depending on the analyzed RH range. A detailed schematic of the setup, consisting of a commercial modular system (MCZ Umwelttechnik), is provided in the Supporting Information, Section S1. Purified air at a constant baseline RH (0 or ∼30%) was used as zero gas (ZG) (MCZ Umwelttechnik, NGA 600−25 MD). The sensors were transiently exposed to increasing RH levels for 4 min, followed by 8 min of ZG. To measure the provided RH levels, a commercial humidity sensor (BME680, Bosch SensorTec) was placed in the test cell and simultaneously read out

https://doi.org/10.1021/acsanm.4c06524
ACS Appl. Nano Mater. 2025, 8, 7428−7439

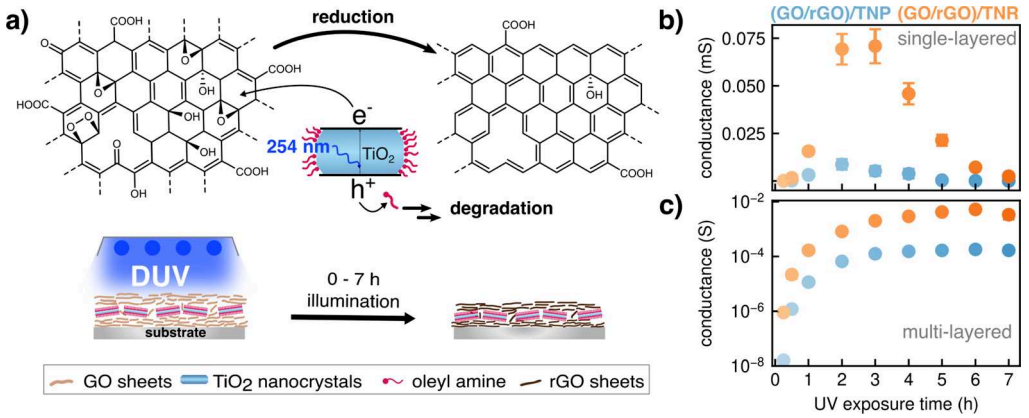

Figure 2. (a) Schematic of the TNC-mediated photocatalytic reduction of GO in GO/TNC hybrid films deposited on a substrate. DUV illumination (254 nm) leads to the excitation of an electron from the valence band to the conduction band of the TNCs. The photoexcited electrons are scavenged by the GO, resulting in the reduction of functional groups and the formation of rGO, while the organic ligands on the TNC surface are oxidized/degraded. (b, c) Evolution of conductance of single-layered (b) and multilayered (c) nanocomposite films with increasing DUV exposure time for (blue) GO/TNP and (orange) GO/TNR films. The error bars represent the standard deviation based on measurements of film areas covering two IDEs on one substrate.

using a Raspberry Pi. The sensors were operated with a bias voltage of 1 V applied by either a Keithley 2601A source meter or an Agilent 4156C semiconductor parameter analyzer, and the resulting current was measured continuously. All time traces were evaluated using a custom-written Python script. The baseline conductance for each sensor was determined by fitting linear functions below each measured transient, taking a ∼30 s interval ∼5 s before RH exposure and a ∼30 s interval after ∼7.4 min of ZG exposure into account as the linear fitting range.

Measurement of Body-Related Humidity. The PI-supported sensor was contacted under ambient conditions using crocodile clips and wires. A constant voltage of 1 V was provided by a Keithley 2601A source meter, and the current was measured.

QCM Measurements. The resistive measurements were combined with gravimetric measurements of hybrid-film-coated QCMs to determine the mass of sorbed water molecules. The measurements were performed using dry purified air as the ZG. The sensors were exposed to a range of RH from ∼0 to 80% using a combined saturator/humidifier system (MCZ Umwelttechnik). The QCMs were contacted using wired sample holders. The baseline resonance frequency of the QCMs was recorded using an Agilent E5100A network analyzer for 100 s in a ZG atmosphere before film deposition and after film deposition and illumination to estimate the mass of the sensing material. During the RH exposure, the resonance frequency of the QCM was continuously monitored using the network analyzer connected via GPIB and controlled by a Python script to readout the (anti)resonance impedance and (anti)resonance frequency.

RESULTS AND DISCUSSION

Hybrid Film Fabrication. Hybrid films were fabricated via an LbL-SC approach from GO and rod- or plate-shaped TNCs. GO was prepared using a modified Hummers method.[31] The hybrid film fabrication process is schematically illustrated in Figure 1a. First, 2 × 25 μL of a methanolic/aqueous GO solution (∼0.1 wt %) was applied onto a rotating substrate, e.g., quartz slides, PI foil, or silicon wafers, followed by the deposition of the TNCs from their colloidal solution in chloroform (0.05−0.4 wt %, 1 × 25 μL), and the subsequent deposition of 2 × 25 μL GO solution, yielding a hybrid film. Due to the high binding affinities of carboxylic acid groups of GO to titania surfaces,[32] the formation of a robust nanocomposite is expected. By repeating the number of alternating deposition cycles (cf. Figure 1a), the film thickness and composition was adjusted. The SEM image (Figure 1a, inset) shows the cross-section of a multilayered GO/TNR hybrid film formed by applying 10 SC deposition cycles.

Figure 1b shows an SEM image of the freeze-dried GO sheets (∼1.1 nm thickness, up to ∼5 μm sheet size, cf. the Supporting Information, Section S3). The TNCs were synthesized following the protocol by Gordon et al.[30] The shape of the nanoparticles is controlled by the choice of the cosurfactant and titanium precursor for the synthesis. The use of $TiCl_4$ results in TNRs, while TiF_4 yields TNPs, due to the stabilization of different crystal facets during TNC growth.[30] Figure 1c,d presents TEM images of brookite/anatase TNRs (∼40 nm length) and anatase TNPs (∼22 nm edge length), respectively. X-ray diffraction (XRD) data of the nanocrystals can be found in the Supporting Information, Section S2. Figure 1e,f shows SEM images of GO/TNP and GO/TNR films deposited on silicon wafers, respectively. At the edges of the film, the incorporation of TNCs between GO layers is clearly seen. The LbL-SC deposition of the films was monitored via UV−vis absorption spectroscopy. Figure 1g,h shows the absorbance spectra of GO/TNP and GO/TNR films deposited on quartz substrates. The spectra were recorded at four different positions of each film and averaged. The shaded areas correspond to the standard deviation of four measurements, indicating a homogeneous film deposition on the substrates. All nanocomposite films show an absorbance maximum at ∼260 nm corresponding to the band gap of the incorporated TNCs, as well as GO characteristic absorbances related to $\pi-\pi^*$ (at 235 nm) and $n-\pi^*$ (at 300 nm) electronic transitions[31,33] (Supporting Information, Sections S2 and S3). Additionally, the TNP-based films showed a shoulder at ∼305 nm. This feature was reported for organically cross-linked TNP composite films[22] and nanocrystalline TiO_2 thin films deposited via chemical vapor deposition and attributed to the quantization of the band structure of the TNCs.[34] The similar increase in absorbance obtained for each SC cycle using TNCs of different shapes suggests a comparable layer formation. Film thicknesses after one SC cycle were determined via AFM analysis (the Supporting Information, Section S4) and were ∼17 and ∼18 nm for the GO/TNP- and GO/TNR hybrid films, respectively. Based on the absorbance measurements, the relative volume fractions of TNPs and TNRs within the films were estimated as 39 and 44%,

https://doi.org/10.1021/acsanm.4c06524
ACS Appl. Nano Mater. 2025, 8, 7428−7439

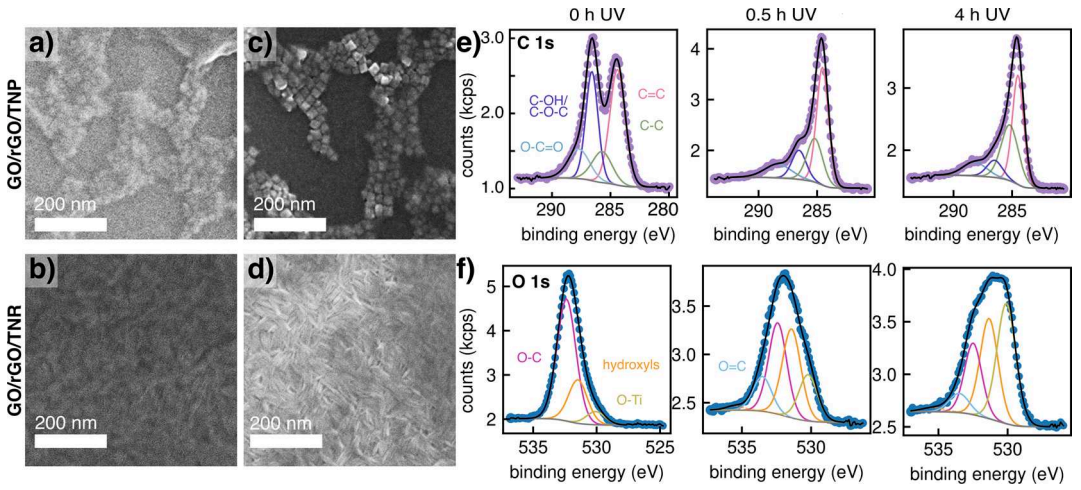

Figure 3. SEM images of (GO/rGO)/TNC films (one LbL-SC cycle) (a, b) before and (c, d) after 7 h DUV illumination. (e) Deconvoluted XP spectra of the C 1s and (f) O 1s core levels for GO/TNP films before and after 0.5 and 4 h DUV exposure.

respectively. The method used to calculate these volume fractions is described in the Supporting Information, Section S4.

Photocatalytic Reduction. The electrical and humidity sensing properties of the GO/TNC films were adjusted by gradually reducing GO via DUV radiation, utilizing the strong photocatalytic activity of the TNCs. The films were illuminated using a DUV radiation source (main emission wavelength of 254 nm and irradiance of 520 mW/cm^2) to match the absorbance of the TNCs. A detailed characterization of the lamp can be found in the Supporting Information, Section S5. The substrate-supported films were irradiated under ambient conditions (i.e., in air) using different exposure times. Figure 2a shows a schematic of the proposed TNC-mediated photocatalytic reduction of GO to rGO. It shows the chemical structure of GO, with both aromatic and sp^3-hybridized regions, in analogy to the Lerf–Klinowski model proposed for the structure of graphite oxide.[35] The basal plane of GO contains functional groups, such as epoxide and hydroxy groups, while carboxy groups are predominantly present at the edges. Upon UV excitation, an electron–hole pair is generated in the TNCs. The photogenerated electrons can reduce the GO, partially restoring the aromatic system. Similar approaches to reducing GO have been reported in previous works. In these earlier studies, GO/titania composites in the liquid phase were illuminated in the presence of ethanol as a hole scavenger, resulting in the accumulation of the photogenerated electrons on the titania surface to reduce the GO.[36] As our experiments were conducted under ambient air, we propose that the amine ligands that stabilize the TNCs (OLAM) serve as hole scavengers and are oxidized and degraded during the photocatalytic reaction (cf. the Supporting Information, Section S8, Figure S12), as has been previously reported for OLAM-stabilized nanocomposites used in photocatalysis.[37,38] For a qualitative assessment, ATR-FTIR spectra of representative drop-cast GO/TNR and GO/TNP films were acquired before and after DUV exposure. With increasing DUV exposure time, the intensity of the bands assigned to the CH_2 stretching modes of OLAM decreased, supporting the suggested mechanism involving the oxidative degradation of the ligand as a sacrificial hole scavenger. Hence, the coverage on the TNC surface with amine ligands can play a role as a limiting factor for the rGO formation. The FTIR spectra are provided in the Supporting Information, Section S6.

The electrical and structural properties of the hybrid films were investigated as a function of the DUV exposure time, TNC type, and hybrid film thickness via charge transport measurements, SEM, and XPS analysis. GO/TNR and GO/TNP films of different thicknesses were deposited onto oxidized silicon wafers with IDEs by varying the number of applied LbL-SC cycles. The films were exposed to DUV radiation for up to 7 h under ambient air. Current–voltage (IV) curves were recorded in specific time intervals. For these measurements, the samples were kept under nitrogen to exclude the sorption of water under ambient humidity. A constant flow of nitrogen was fed through the measurement cell by using a commercial test gas system for at least 1 min until a stable baseline resistance was achieved. The applied voltage was swept between ±1 V and the resulting current was measured using a sourcemeter. All films exhibited ohmic IV characteristics. The conductance was extracted as the slope of the linear curves. Figure 2b shows the evolution of the conductance for (GO/rGO)/TNP (blue) and (GO/rGO)/TNR films (orange) with an increasing DUV exposure time. These films were prepared by applying only one LbL-SC cycle. For both types of films, an increase in conductance can be observed with the onset of DUV exposure, indicating the formation of the rGO and the restoration of conductive sp^2-hybridized regions. For comparison, Figure 2c shows the evolution of conductance with increasing DUV exposure times for multilayered (GO/rGO)/TNR (orange) and (GO/rGO)/TNP (blue) films. Overall higher conductances were observed for the (GO/rGO)/TNR films than for TNP-based films. For the single-layered TNR film, the conductance was up to 8 times higher than for the corresponding TNP film. A maximum in conductance can be observed for the single-layered films, followed by a steady decrease with increasing DUV exposure time. We attribute this decrease in conductance to the reoxidation and the photocatalytic degradation of the rGO/GO network with prolonged DUV exposure. Similar effects were reported for the reduction of GO sheets attached to titania nanoparticles in ethanol[39] or water and explained by the initial formation of rGO followed by its degradation to smaller fragments and finally to carbon dioxide.[40] In the case of the (GO/rGO)/TNP thin film, the maximum conductance

https://doi.org/10.1021/acsanm.4c06524
ACS Appl. Nano Mater. 2025, 8, 7428–7439

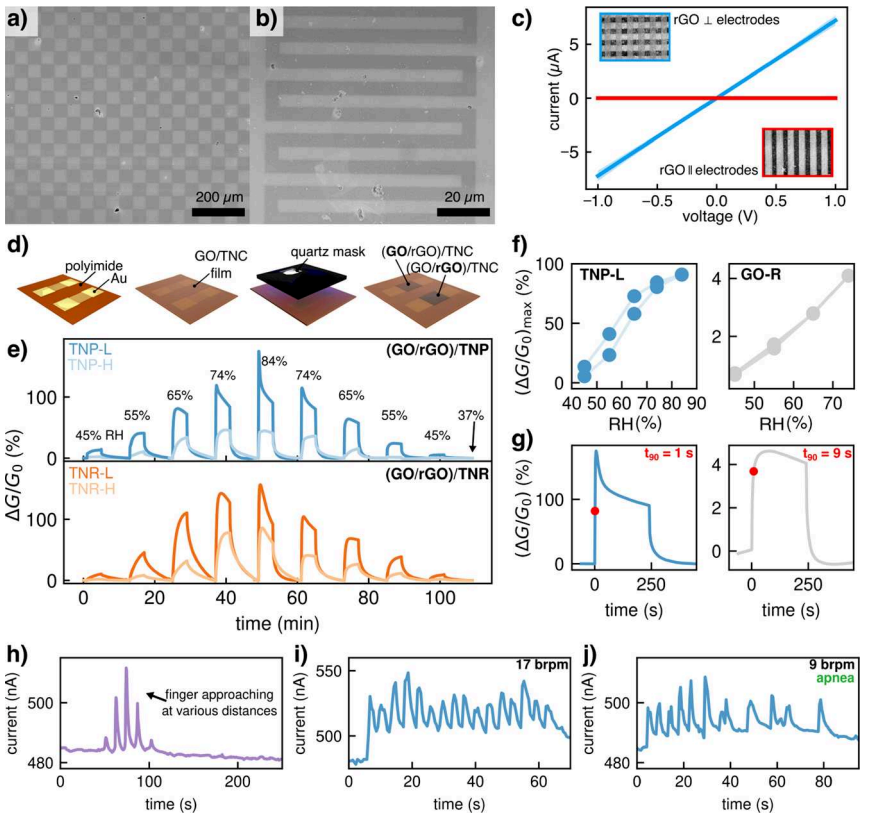

Figure 4. (a, b) Optical micrographs of photocatalytically patterned rGO/GO: (a) checkerboard pattern and (b) meander pattern. (c) IV curves of a (GO/rGO)/TNR film measured after DUV illumination (1 h) through a mask producing conductive rGO stripe patterns connecting the IDEs (blue) and not connecting the electrode fingers (red). The insets show photographs of the respective stripe patterns and electrode fingers. (d) Fabrication process of photocatalytically patterned (GO/rGO)/TNC sensors on PI substrates equipped with IDEs. (e) Baseline-corrected relative conductance change of (GO/rGO)/TNP (blue) and (GO/rGO)/TNR (orange) films (four LbL-SC cycles) with adjusted degree of reduction to transient (4 min) variations in RH from a baseline humidity of ∼37%. All measurements were conducted at room temperature. (f) Response isotherms of the TNP-L (30 min DUV exposure) sensor (blue) and the GO-R (120 min DUV exposure) sensor (gray) and (g) respective transient responses to 74% RH used to extract the response times. (h–j) Real-time body-related humidity sensing using the TNP-L sensor for (h) the detection of finger approximation at varying distances (∼0.5 cm distance to the substrate), (i) determination of a healthy breathing rate when breathing in proximity to the sensor, and (j) detection of an interrupted breathing pattern.

was reached after ∼2 h of DUV exposure, and after ∼3 h in the case of the corresponding (GO/rGO)/TNR thin film (Figure 2b). According to our above-mentioned discussion, the lower mass fraction of organic ligands on the TNP surface compared to the TNRs, assessed via TG analysis (cf. the Supporting Information, Section S2) is considered to be a limiting factor for the rGO formation. This can lead to the premature degradation of rGO once the organic ligand is consumed. In the case of the multilayered hybrids, the conductance reaches saturation after a few hours of DUV exposure (Figure 2c). After several hours of DUV exposure, however, a slight decrease in conductance was observed. The higher conductance of the TNR-based films compared to the TNP-based films is most likely related to the smaller dimensions of the TNRs. Due to their higher surface-to-volume ratio, the TNRs offer more interfacial contact points to GO than the TNPs. Therefore, the reduction to rGO can occur more uniformly throughout the GO layer.[41] In addition, the TNCs have different crystal structures and exposed facets, imparting different photocatalytic efficiencies. The anatase TNPs exhibit high fractions of {001} facets, which have high photocatalytic activity.[30,42] The TNRs are obtained in a brookite/anatase mixture. Some studies suggest that brookite shows superior photocatalytic activity in certain applications.[43,44] We also varied the TNC concentration within the hybrid films (Supporting Information, Section S7) resulting in (i) increased rates of reduction and (ii) higher conductances for higher TNC concentrations. Reference experiments in which pure GO films were exposed to DUV light confirmed the enhancement and acceleration of rGO formation in the presence of a TNC photocatalyst (Supporting Information, Section S8). Generally, our findings demonstrate that the conductance of (GO/rGO)/TNC hybrid films can be enhanced and tuned over several orders of magnitude by DUV illumination and by variation of the TNC catalyst, as well as the film thickness.

Figure 3a–d shows SEM images of (GO/rGO)/TNP- and (GO/rGO)/TNR-based thin films (one LbL-SC cycle) deposited on silicon substrates before (a, b) and after (c, d) 7 h DUV exposure. The TNRs are more evenly distributed over the film area than the TNPs. Hence, the photocatalytic reduction of GO can occur more homogeneously within the GO layer enabling overall higher conductances of the (GO/rGO)/TNR films compared to the (GO/rGO)/TNP films, as discussed earlier. In general, the TNC distribution depends on the TNC size, shape, and organic content of the films (Supporting Information, Section S2). Further, the SEM images shown in Figure 3a–d reveal a change in the film

https://doi.org/10.1021/acsanm.4c06524
ACS Appl. Nano Mater. 2025, 8, 7428–7439

composition with increasing DUV exposure time. The contrast of the underlying TNCs increases with prolonged DUV exposure, supporting the proposed degradation of the initially formed rGO over time.

The composition and chemical changes induced in the films by the photocatalytic reduction were further characterized via XPS analysis. Figure 3e shows XPS spectra of the C 1s core levels of GO/TNP thin films (one LbL-SC cycle) before (0 h) and after 0.5 and 4 h DUV exposure. The signals were fitted using 4 Gaussians corresponding to C−C, C═C carbon and different oxidized carbon species. The envelope functions are plotted as solid black lines, and the background as gray lines. The peak centered at 284.5 eV (light pink line) corresponds to sp^2-hybridized C═C-bonds.[33] Peaks corresponding to oxidized carbon species are located at higher binding energies, such as C−O bonds in hydroxy/epoxy groups (purple line) at 286 eV, C═O bonds (light blue line) at 288 eV,[33] as well as sp^3-hybridized C−C-bonds (green line) at 285.5 eV. With increasing DUV exposure time, the peak intensity and area corresponding to C−OH/C−O−C decrease, while the peak assigned to C═C bonds increases, confirming the formation of rGO and the removal of oxygen-containing functional groups. Bell et al. reported the selective removal of epoxy- and hydroxy groups in photocatalytically reduced GO.[28] Figure 3f shows the O 1s core-level spectra of the same films. The peaks at 532−533 eV can be assigned to the O−C/O═C bonds (pink and light blue lines) present in functional groups in GO, while peaks at lower energies are assigned to the metal oxide Ti−O bonds (orange line) and hydroxyls (orange line). The Ti 2p core-level spectra were also measured and can be found in the Supporting Information, Section S9. XPS spectra of (GO/rGO)/TNP films recorded for the N 1s core levels indicate the removal of the amine group by decreasing peak intensity with an increasing DUV exposure time. However, the rather low signal-to-noise ratio does not enable a quantitative analysis (Supporting Information, Section S9). Spectra of analogous TNR-based films revealed the same trends as shown in Figure 3 and are provided in the Supporting Information, Section S9. Additional characterization of the photocatalytic reduction was performed by FTIR spectroscopy. The corresponding data can be found in the Supporting Information, Section S6. Briefly, the measurements are in agreement with the XPS data, demonstrating the formation of rGO. FTIR analysis qualitatively indicates the removal of the epoxy and hydroxy groups.

Photocatalytic Lithography and Flexible Humidity Sensors. The reduction method was applied to pattern (GO/rGO)/TNC films via photocatalytic lithography. This approach enables the fabrication of resistive RH sensors with selectively tuned GO/rGO ratios and, hence, adjustable electrical properties and sensitivity to water. For this purpose, multilayered hybrid films were deposited on silicon wafers and exposed through a patterned quartz mask. Figure 4a,b shows optical microscopy images of a (GO/rGO)/TNR thin film (four LbL-SC cycles) after DUV exposure (1 h) through a photomask with a checkerboard pattern and meander structure. Differences in contrast indicate the selective reduction of GO on the DUV exposed areas (dark areas). To verify the spatially resolved reduction, hybrid films (four LbL-SC cycles) were deposited on IDEs and illuminated through a photomask with stripes (20 μm width) aligned either perpendicular or parallel to the IDEs. Figure 4c shows the resulting IV curves, demonstrating that DUV exposure perpendicular to the IDEs leads to a significant increase in conductivity, confirming the formation of conductive rGO patterns connecting the IDE fingers, as shown by the microscopy image in the inset, top left. For DUV exposure parallel to the IDEs, no significant increase in the measured current was observed, confirming the selective reduction of GO to only the exposed areas.

Figure 4d shows a scheme of the fabrication of resistive sensors with a variable degree of reduction on flexible PI substrates via photocatalytic patterning. Multilayered hybrid films containing GO and TNPs or TNRs (four LbL-SC cycles) were fabricated following the method illustrated in Figure 1a. First, GO/TNC films were deposited on plasma-treated PI substrates equipped with two IDE structures. Film sections on the IDE structures were selectively exposed to DUV light through a quartz mask. The exposure time was adjusted, depending on the desired degree of reduction. Next, the mask was rotated by 180° and the film covering the second IDE area was exposed to DUV light. Likewise, pairs of sensors with adjusted GO/rGO ratios, i.e., a higher degree of reduction (H) and a lower degree of reduction (L) were obtained. Depending on the incorporated TNCs, the DUV exposure time was adjusted for each film area to obtain comparable baseline conductances for TNP- and TNR-based films. Multilayered films were used as resistive sensors since they enable higher conductances and also allow for tuning the GO/rGO ratio more precisely. Table 1 summarizes the as-fabricated sensor compositions and the applied DUV exposure times. A film of pristine GO, fabricated using the same amount of GO as in four LbL-SC cycles for GO/TNC composite films (10 × 25 μL of GO solution), was illuminated for 2 h with DUV light to form rGO and measured as a reference sensor (GO-R).

Table 1. Hybrid Films for Resistive RH Sensing

sensor name	composition	DUV exposure (min)
TNP-L	(GO/rGO)/TNP	30
TNP-H	(GO/rGO)/TNP	120
TNR-L	(GO/rGO)/TNR	25
TNR-H	(GO/rGO)/TNR	60
GO-R	(GO/rGO)	120

To study the sensors' resistive responses to RH, two films were placed into a test cell connected to a commercial gas calibration system, equipped with a ZG system to provide purified air and two humidification units to provide humidified ZG and humidified AG. The sensors were operated at a constant bias voltage of 1 V, and the resulting currents were measured. Purified air with a baseline humidity of ∼37% RH was used as the ZG to simulate the typical lower RH level of indoor air. The sensors were transiently exposed to increasing RH (∼45−55−65−74−84%, and back) for 4 min, followed by exposure to ZG for 8 min. A commercial gas and humidity sensor inside the test cell was used as a reference sensor. The data of the commercial reference sensor can be found in the Supporting Information, Section S10. The relative conductance change $\Delta G/G_0$, defined by eq 1, was extracted as sensor signal from the recorded $I(t)$ traces, with $G = I/V$.

$$\frac{\Delta G}{G_0} = \left[\frac{G(t)}{G_0(t)} - 1\right] \times 100\% \quad (1)$$

https://doi.org/10.1021/acsanm.4c06524
ACS Appl. Nano Mater. 2025, 8, 7428−7439

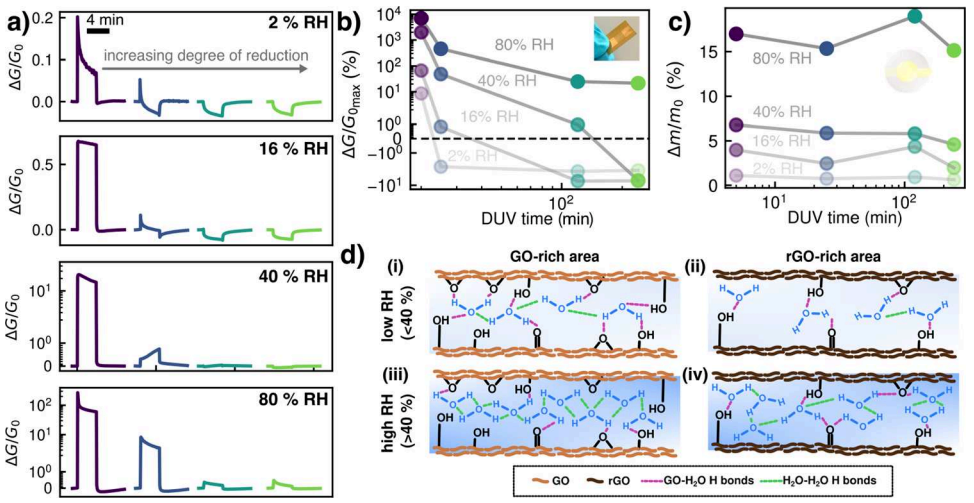

Figure 5. (a) Baseline-corrected response transients of (GO/rGO)/TNP chemiresistors tuned by varying the DUV exposure time (20, 25, 120, 240 min) to different RH levels. (b) Relative conductance change for selected RH levels (2, 16, 40, 80%) after 4 min exposure as a function of DUV exposure time. The inset shows a photograph of a flexible chemiresistor on PI foil. (c) Relative mass uptake of (GO/rGO)/TNP films deposited on QCM transducers for selected RH levels as a function of the DUV exposure time. (d) Humidity sensing mechanism proposed for sensors with adjusted GO/rGO ratios. (i) At low RH levels (<40%), in GO-rich areas, a high density of polar functional groups act as sorption sites for water molecules that interact via H-bonds (pink dashed lines), contributing proton hopping sites additionally to intermolecular water H-bonds (green dashed lines), facilitating the formation of paths of ionic conductivity. (ii) In rGO-rich areas, water molecules cannot form ionic conductive chains, and act as an electron donor, attenuating the hole-based rGO charge transport. (iii, iv) At higher RH levels (>40%), secondary water sorption leads to intermolecular hydrogen bonds and predominant ionic conductivity for both sensor types.

where G_0 is the baseline conductance. Figure 4e shows baseline-corrected sensor responses of the TNP-based sensors (blue traces) and the TNR-based sensors (orange traces). The timetrace of the GO-R reference film can be found in the Supporting Information, Section S8. All sensors responded with an increase in conductance with increasing RH levels. At high RH, an increase in conductance has been reported for GO[19] that is attributed to sorption of water molecules on the hydrophilic GO structure, forming chains of ionic conductivity.[21] Here, hydroxy and epoxy groups provide proton hopping sites for water conductivity according to the Grotthuss mechanism.[19,45−47] The films with lower degree of reduction show higher response amplitudes arising from the higher number of polar functional groups providing sorption sites for water molecules.[48,49] Figure 4f shows the relative conductance changes after 4 min of transient exposure to increased RH of the TNP-L sensor and the GO-R sensor, for different RH levels. While the GO-R reference sensor shows little hysteresis and good linearity in the applied RH range, the response amplitude is enhanced by a factor of ∼20 for the TNP-L film. The TNCs may provide additional sorption sites for water molecules, and the intercalation of TNCs between GO sheets can yield a larger overall surface area with accessible sorption sites for water molecules, compared to the pure GO/rGO film.[48] Response times t_{90}, corresponding to the time needed to reach 90% of the relative conductance change after 4 min, were determined for the TNP-L and GO-R sensor at ∼70% RH. The GO-R sensor had a response time of 9 s, while the TNP-L sensor had the shortest response time t_{90} = 1.5 s, averaged over both 74% RH transients (Figure 4g). As can be seen from the time traces shown in Figure 4e, generally longer response times were obtained with an increasing degree of reduction. While the GO-R sensor shows fast and reproducible responses to RH level changes, the hybrid films, especially the (GO/rGO)/TNP films, surpass the GO-R film in terms of boosted sensitivity, faster responses at high RH, and greater efficiency regarding fabrication time. Further, the sensor performance—in terms of sensitivity and response times—is comparable or superior to GO/rGO-based resistive RH sensors presented in the literature, as summarized in the Supporting Information, Section S11, Table S2. To test the reproducibility of the sensor performance of TNP-L and TNP-H films, duplicate films were exposed to RH changes. Again, TNP-L films have higher response amplitudes and faster response times than the TNP-H films. Differences in the response amplitudes arise from film-to-film variations during the same UV exposure times, where the desired reduction degree can be adjusted by monitoring the baseline conductivity. The data are provided in the Supporting Information, Section S12. The long-term stability and sensing performance of the TNP-L sensor (Figure 4e) were evaluated after more than two years. Following extended storage in ambient air, the sensor was exposed to varying RH levels, as shown in the Supporting Information, Figure S22. After this period, a change in sensing behavior was observed, most notably in response kinetics. Nevertheless, the sensor maintained high sensitivity, exhibiting relative conductance changes of up to 50% in response to RH variations from 30% (baseline RH) to 70%. In addition, we tested the repeatability of the sensor responses of a freshly prepared sensor after bending the flexible substrate, where we observed a tendency of decreasing responses to RH changes after repeated twisting/bending of the substrates (the Supporting Information, Section S12).

Due to its high sensitivity and short response times, the TNP-L sensor was tested for potential body-related humidity sensing, such as skin-humidity-based proximity sensing and respiration monitoring. Figure 4h shows the change in the sensor current when a finger approached the film surface at varying distances during the first ∼100 s. Clear differences in amplitude for varying distances can be seen. Figure 4i displays the recorded sensor current during the exposure to exhaled breath, which, according to the literature, has humidity levels

https://doi.org/10.1021/acsanm.4c06524
ACS Appl. Nano Mater. 2025, 8, 7428−7439

ranging between 42−91% and a temperature between 31.4−34.8 °C.[50] Breathing in proximity to the film resulted in an increase in the current. The recorded time trace demonstrates that the response and recovery times are sufficiently fast to resolve a healthy breathing rate of 17 breaths per minute (brpm). As shown in Figure 4j, it was possible to detect a pathological breathing rate of 9 brpm of an interrupted breathing pattern which is of diagnostic relevance, e.g., in apnea diagnosis.

Sensing Mechanism. To analyze the RH sensing characteristics of the (GO/rGO)/TNP flexible sensors in more detail, the resistive responses of composite films of varying degrees of reduction (∼20 to 240 min DUV treatment) were studied by applying a wider range of RH levels (0.95 to 79%). These measurements were combined with gravimetric measurements to determine the mass uptake of water molecules into the hybrid films. Here, QCM sensors (f_0 ∼ 10 MHz, AT-cut, Au electrodes) were coated on one side with (GO/rGO)/TNP films via the LbL-SC procedure, and exposed to DUV light for different times, so that both the resistive and gravimetric sensors include hybrid films of gradually increasing degrees of reduction to enable a qualitative comparison. The coated QCMs and the resistive sensors were placed in the same test cell and exposed to different RH levels. Purified air (0% RH) was used as ZG. RH levels of up to ∼27% were provided using a gas calibration system with a vapor saturation unit, while higher RH levels (>40%) were provided using the commercial humidification module. The RH levels were set to ∼0.95, 2.2, 4.0, 8.3, 16, 27, 42, 61, and 79%.

Figure 5a shows selected baseline-corrected resistive transient responses to different RH levels. At low RH changes (2%), the sensor with the highest GO content shows a positive signal response, in agreement with the RH responses measured at a higher baseline RH (see above). On the other hand, the sensors of higher degrees of reduction (increasing from left to right) exhibit negative signals of down to −5%. An increase in resistance during RH exposure has been reported in the literature for rGO, and was attributed to perturbations of the p-type conductivity of rGO. Water can act as an electron donor, resulting in a decrease of charge carrier density.[51,52] For increasing RH transient exposures, the negative sensor signals invert and become positive (Figure 5b). The RH value of inversion depends on the degree of reduction: For instance, at 16% RH, two resistors of high GO content show a positive signal of up to ∼60%, while the sensors that experienced longer UV exposure, still respond with negative signals of −7%, each. Finally, at a higher RH level (∼80%), all sensors show positive responses. In the low RH range up to ∼40%, the sensor with the highest degree of reduction shows only negative responses, while films with more GO content show signal inflection points at lower RH values, demonstrating the ability to tailor and optimize the RH sensing ranges of the material. A similar trend with a point of inversion was reported by Tai et al. for rGO humidity sensors obtained by gradual thermal reduction for up to 13 h.[20] At high RH (∼80%), the sensors exposed to DUV light for 2 and 4 h show similar response amplitudes, as well as almost identical baseline resistances, suggesting that the saturation conductance attainable via the photocatalytic reduction was reached for these films (Figure 2c). The films with high rGO content, however, showed pronounced baseline drifts at very high RH (e.g., ∼80%). We attribute this finding to the spontaneous condensation of water on the films. The time traces for all resistors can be found in the Supporting Information, Section S13.

The resistive sensing characteristics were complemented by microgravimetric measurements to determine the amount of sorbed water at different GO/rGO ratios within the hybrid films. Using the Sauerbrey equation (eq 2),[53] the change in mass Δm caused by water sorption can be calculated from the measured shift of the resonance frequency Δf,

$$\Delta m = -\Delta f \frac{\sqrt{\mu\rho}}{2f_{0,f}^2} A_{QCM} \tag{2}$$

with μ and ρ being the shear modulus (29.47 GPa) and the density (2.65 g/cm^3) of quartz, $f_{0,f}$ is the resonance frequency of the coated QCMs, and A_{QCM} is the sensitive area (0.2043×10^{-4} m^2). After film deposition and DUV exposure, the mass of the hybrid films (four LbL-SC cycles) was calculated using this equation, under consideration of the frequency shift Δf after film deposition with regard to the resonance frequency of the bare QCM. The masses of the films ranged between ∼1.7 and 2.3 μg, with the highest mass determined for the film with the lowest degree of reduction. In accordance with our observations discussed above (cf. Figure 3a−d) we attribute the reduced mass after DUV exposure to the decomposition of the ligands on the TNC surface as well as the removal of GO functional groups. All coated QCMs showed a shift of resonance frequency of up to 400 Hz when exposed to humidified air (cf. the Supporting Information, Section S14). The water sorption and desorption was fast and reversible, as shown by the rectangular transient shapes and the stable baseline frequencies. The relative mass uptake $\Delta m/m$ of the films was determined for all tested RH levels. Figure 5c shows the mass uptake for selected RH levels as a function of the UV exposure time of the sensors. Here, no distinct trend of the relative mass change with an increasing degree of GO reduction of the films is observed. The RH level-dependent sorption isotherms (cf. Supporting Information, Section S14) resemble type II isotherms, corresponding to unrestricted monolayer-multilayer sorption to the material at high RH levels.[54] These findings indicate that secondary water sorption occurs at RH levels >40%, leading to multilayered water films. The maximum relative mass uptake for all films, regardless of their degree of reduction, is ∼17%. Hence, the distinct resistive responses of the films to RH are not caused by varying amounts of sorbed analyte but have to be attributed to specific interactions of water molecules with the internal chemical structure of the composites, as well as their different electrical properties. A schematic of the proposed sensing mechanism at different RH levels for (i, iii) GO- and (ii, iv) rGO-rich hybrids is illustrated in Figure 5d. (i) GO-rich films provide a high density of polar binding sites, such as epoxy and hydroxy groups, that allow for water sorption via H-bonds (pink dashed lines). The chemisorbed water molecules form a percolation path of ionic conductivity (green dashed lines) involving the GO's functional groups acting as additional proton hopping sites. This effect results in the enhanced conductivity of the low-conductive material. (ii) Films with a higher fraction of rGO, however, exhibit a lower density of hydroxy and epoxy groups. At the same time, the restored sp^2 system imparts an enhanced baseline conductance. Commonly, the rGO is described as a p-type conductor. Water acts as electron donor, interfering with the hole-dominated charge transport, resulting in an increase of resistance.[51] At low RH, the sorbed

https://doi.org/10.1021/acsanm.4c06524
ACS Appl. Nano Mater. 2025, 8, 7428−7439

water molecules cannot form an extended network throughout the material. Although a certain degree of ionic conductivity may be established in these films also at lower RH, the resulting increase of conductance is hidden by the overall higher baseline conductance and superimposed by attenuated hole transport. Mixed sensor responses are attributed to balancing the opposing effects for intermediate degrees of reduction. (iii, iv) Finally, at high RH levels, secondary water layers are physisorbed, in all types of films. Hence, the conductance via the Grotthuss mechanism becomes predominant, resulting in an overall increase of conductance.

SUMMARY AND CONCLUSIONS

In this study, we investigated nanostructured GO/TNC hybrid films and their tunability via TNC-mediated photocatalytic GO reduction for resistive RH sensing. We introduced an LbL-SC method to fabricate uniform layered nanofilms on flexible and rigid substrates using GO and anatase TNPs or anatase/brookite TNRs. The film thickness (15−150 nm) was adjusted by varying the number of LbL-SC deposition cycles. The film composition was tuned via DUV illumination, exploiting the photocatalytic activity of the TNCs. We systematically studied the influence of key parameters on the photocatalytic reduction, such as varying the TNC catalyst, DUV exposure time, and film thickness. Exposing the films to DUV light for up to 2 h in the presence of a TNC catalyst resulted in an enhancement of an order of magnitude in the obtained conductance compared to pristine GO layers exposed to DUV radiation for the same duration. Compared with TNP-based films, a stronger photocatalytic enhancement and generally higher conductances were obtained for TNR-based nanocomposites. Depending on the film thickness, the obtained conductance reached a constant value or decreased with prolonged DUV exposure. This progression was investigated by XPS and SEM measurements, confirming the tunable GO/rGO and (GO/rGO)/titania nanoparticle ratio. Finally, we prepared photocatalytically patterned (GO/rGO)/TNC nanofilms of varying degrees of reduction and tested the effect of the photocatalytic reduction on the nanocomposites' resistive humidity sensing ability in different environments. At a high baseline humidity of ∼30−40%, all films responded with a positive change in conductance to increasing RH levels. (GO/rGO)/TNP-based films with higher GO content showed the most promising sensing performance exhibiting the shortest response times of down to 1 s, low hysteresis, and high sensitivities. Future studies will address the aging behavior and long-term stability of the sensors. These films were also suitable to detect physiological changes in RH such as breathing patterns and skin moisture. The sensing range was adjusted by varying the time of the DUV exposure. The (GO/rGO)/TNP films were exposed to lower RH levels (1−80%) using dry air (0% RH) as reference gas. Depending on (i) the RH level and (ii) the GO/rGO ratio, the resistive responses transitioned from negative to positive conductance changes, while the relative mass uptake of water was constant at a given RH level for all tested films, as revealed by parallel QCM measurements.

In conclusion, the use of TNC-mediated photocatalytic reduction is an efficient method to obtain optimized GO/rGO ratios in nanostructured thin films for humidity sensor applications. These films exhibit tunable humidity sensing properties, with rGO-rich nanocomposites performing best at low RH levels and GO-dominant at high RH. This highlights the potential for the fabrication of GO-based humidity sensors with tunable sensing properties, and their use, e.g., as ratiometric sensors or in applications requiring specific detection ranges.

ASSOCIATED CONTENT

Supporting Information

The Supporting Information is available free of charge at https://pubs.acs.org/doi/10.1021/acsanm.4c06524.

TNC characterization (XRD, TGA), GO characterization (AFM, UV−vis, FTIR spectrscopy), estimation of GO and TNC content in hybrid films, characterization of DUV radiation source, spectroscopic characterization of photocatalytically reduced (GO/rGO)/TNC films (FTIR spectroscopy), TNC concentration-dependent reduction, reference experiments of DUV-induced GO reduction of pure GO films (IV curves, FTIR spectroscopy, AFM, humidity sensing), additional XPS data of (GO/rGO)/TNR films, reference humidity measurements with a commercial sensor, comparison of sensor performance with GO/rGO resistive sensors reported in the literature, resistive sensor time traces, QCM sensor time traces, and long-term stability and reproducibility measurements (PDF)

AUTHOR INFORMATION

Corresponding Authors

Sophia C. Bittinger − *Institute of Physical Chemistry, University of Hamburg, 20146 Hamburg, Germany;* Present Address: CIC biomaGUNE, Basque Research and Technology Alliance (BRTA), 20014 Donostia-San Sebastian, Spain; orcid.org/0000-0002-7735-948X; Email: sophia.caroline.bittinger@uni-hamburg.de

Tobias Vossmeyer − *Institute of Physical Chemistry, University of Hamburg, 20146 Hamburg, Germany;* orcid.org/0000-0001-9738-3826; Email: tobias.vossmeyer@uni-hamburg.de

Authors

Jana Struck − *Institute of Physical Chemistry, University of Hamburg, 20146 Hamburg, Germany;* orcid.org/0000-0002-0251-0579

Finn Dobschall − *Institute of Physical Chemistry, University of Hamburg, 20146 Hamburg, Germany;* orcid.org/0009-0000-6900-8236

Sophie Benthien − *Institute of Physical Chemistry, University of Hamburg, 20146 Hamburg, Germany*

Hauke Hartmann − *Institute of Physical Chemistry, University of Hamburg, 20146 Hamburg, Germany;* orcid.org/0000-0002-2912-4862

Hendrik Schlicke − *Fraunhofer Center for Applied Nanotechnology CAN, 20146 Hamburg, Germany;* Present Address: Institute of Physical Chemistry and Polymer Physics, Leibniz Institute of Polymer Research Dresden, Hohe Strasse 6, 01069 Dresden, Germany; orcid.org/0000-0002-6977-4042

Mona Kohantorabi − *Centre for X-ray and Nano Science (CXNS), Deutsches Elektronen-Synchrotron (DESY), 22607 Hamburg, Germany;* orcid.org/0000-0002-4230-8797

Heshmat Noei − *Centre for X-ray and Nano Science (CXNS), Deutsches Elektronen-Synchrotron (DESY), 22607 Hamburg, Germany;* orcid.org/0000-0003-1294-3527

https://doi.org/10.1021/acsanm.4c06524
ACS Appl. Nano Mater. 2025, 8, 7428−7439

Complete contact information is available at:
https://pubs.acs.org/10.1021/acsanm.4c06524

Author Contributions

T.V. and S.C.B. proposed and developed the research idea. S.C.B. did the experimental design and carried out major parts of the experimental work and data analysis. J.S. synthesized the TNRs and optimized the TNR/GO film deposition. The photocatalytic reduction experiments and setup were developed by H.S., S.C.B. and H.H., and the materials' characterization was performed by J.S., H.H., and S.C.B. S.B. carried out the photocatalytic patterning experiments. F.D. performed additional humidity sensing measurements and data analysis and characterized the UV source. XPS measurements and data analysis were done by M.K. and H.N. The manuscript was written by S.C.B. and T.V. The project was supervised by T.V.

Notes

The authors declare no competing financial interest.

■ ACKNOWLEDGMENTS

The authors acknowledge the financial support from the Open Access Publication Fund of University Hamburg. The authors thank the electron microscopy service unit at the University of Hamburg, especially Robert Schön, Dr. Charlotte Ruhmlieb, and Stefan Werner for SEM and TEM measurements. Gefördert durch die Deutsche Forschungsgemeinschaft (DFG) - 395896547; 408076438. Funded by the Deutsche Forschungsgemeinschaft (DFG, German Research Foundation) - 395896547; 408076438.

■ REFERENCES

(1) Duan, Z.; Jiang, Y.; Tai, H. Recent Advances in Humidity Sensors for Human Body Related Humidity Detection. *J. Mater. Chem. C* **2021**, *9*, 14963−14980.
(2) Delipinar, T.; Shafique, A.; Gohar, M. S.; Yapici, M. K. Fabrication and Materials Integration of Flexible Humidity Sensors for Emerging Applications. *ACS Omega* **2021**, *6*, 8744−8753.
(3) Zhang, D.; Wang, M.; Tang, M.; Song, X.; Zhang, X.; Kang, Z.; Liu, X.; Zhang, J.; Xue, Q. Recent progress of diversiform humidity sensors based on versatile nanomaterials and their prospective applications. *Nano Res.* **2023**, *16*, 11938−11958.
(4) Montes-García, V.; Samorì, P. Humidity Sensing with Supramolecular Nanostructures. *Adv. Mater.* **2023**, *36*, No. 2208766.
(5) Su, C.-H.; Chiu, H.-L.; Chen, Y.-C.; Yesilmen, M.; Schulz, F.; Ketelsen, B.; Vossmeyer, T.; Liao, Y.-C. Highly Responsive PEG/Gold Nanoparticle Thin-Film Humidity Sensor via Inkjet Printing Technology. *Langmuir* **2019**, *35*, 3256−3264.
(6) Li, J.; Zhou, Y.; Wang, Y.; Zhou, S.; Zhang, R.; Wang, Y.; Zang, Z. Improving Humidity Sensing of Black Phosphorus Nanosheets by Co-Doping Benzyl Viologen and Au Nanoparticles. *J. Electrochem. Soc.* **2022**, *169*, No. 017513.
(7) Wang, Y.; Zhou, Y.; Xie, G.; Li, J.; Wang, Y.; Liu, X.; Zang, Z. Dual Resistance and Impedance Investigation: Ultrasensitive and Stable Humidity Detection of Molybdenum Disulfide Nanosheet-Polyethylene Oxide Hybrids. *ACS Appl. Interfaces* **2021**, *13*, 25250−25259.
(8) Zhang, Q.; Zhang, J.; Wan, S.; Wang, W.; Fu, L. Stimuli-Responsive 2D Materials Beyond Graphene. *Adv. Funct. Mater.* **2018**, *28*, No. 1802500.
(9) Liang, R.; Luo, A.; Zhang, Z.; Li, Z.; Han, C.; Wu, W. Research Progress of Graphene-Based Flexible Humidity Sensor. *Sensors* **2020**, *20*, 5601.
(10) Shojaee, M.; Nasresfahani, S.; Dordane, M.; Sheikhi, M. Fully integrated wearable humidity sensor based on hydrothermally synthesized partially reduced graphene oxide. *Sens. Actuators A: Phys.* **2018**, *279*, 448−456.
(11) Anichini, C.; Aliprandi, A.; Gali, S. M.; Liscio, F.; Morandi, V.; Minoia, A.; Beljonne, D.; Ciesielski, A.; Samorì, P. Ultrafast and Highly Sensitive Chemically Functionalized Graphene Oxide-Based Humidity Sensors: Harnessing Device Performances via the Supramolecular Approach. *ACS Appl. Mater. Interfaces* **2020**, *12*, 44017−44025.
(12) Jiang, Y.; Ma, J.; Shen, L.; Zhang, W.; Yang, K.; Zhu, B.; Yang, Y.; Ma, H.; Chen, X.; Bai, S.; Zhu, N. Chemresistor Smart Sensors from Silk Fibroin-Graphene Composites for Touch-free Wearables. *ACS Appl. Mater. Interfaces* **2023**, *15*, 47196−47207.
(13) Cho, H.; Lee, C.; Lee, C.; Lee, S.; Kim, S. Robust, Ultrathin, and Highly Sensitive Reduced Graphene Oxide/Silk Fibroin Wearable Sensors Responded to Temperature and Humidity for Physiological Detection. *Biomacromolecules* **2023**, *24*, 2606−2617.
(14) Ma, R.; Tsukruk, V. V. Seriography-Guided Reduction of Graphene Oxide Biopapers for Wearable Sensory Electronics. *Adv. Funct. Mater.* **2017**, *27*, No. 1604802.
(15) Yuan, Y.; Peng, B.; Chi, H.; Li, C.; Liu, R.; Liu, X. Layer-by-layer inkjet printing SPS:PEDOT NP/RGO composite film for flexible humidity sensors. *RSC Adv.* **2016**, *6*, 113298−113306.
(16) Noh, W.; Go, Y.; An, H. Reduced Graphene Oxide/Polyelectrolyte Multilayers for Fast Resistive Humidity Sensing. *Sensors* **2023**, *23*, 1977.
(17) Kumar, A.; Kumar, A.; Varma, G. D. Ultrafast Resistive-Type γ-Fe_2O_3−rGO Nanohybrid-Based Humidity Sensor − a Respiratory Monitoring Tool. *J. Mater. Chem. C* **2021**, *9*, 8002−8010.
(18) Jung, I.; Dikin, D. A.; Piner, R. D.; Ruoff, R. S. Tunable Electrical Conductivity of Individual Graphene Oxide Sheets Reduced at "Low" Temperatures. *Nano Lett.* **2008**, *8*, 4283−4287.
(19) Wee, B.-H.; Khoh, W.-H.; Sarker, A. K.; Lee, C.-H.; Hong, J.-D. A High-Performance Moisture Sensor Based on Ultralarge Graphene Oxide. *Nanoscale* **2015**, *7*, 17805−17811.
(20) Tai, Y.; Bera, T. K.; Lubineau, G.; Yang, Z. Combining the converse humidity/resistance response behaviors of rGO films for flexible logic devices. *Journal of Materials Chemistry C* **2017**, *5*, 3848−3854.
(21) Popov, V. I.; Nikolaev, D. V.; Timofeev, V. B.; Smagulova, S. A.; Antonova, I. V. Graphene-Based Humidity Sensors: The Origin of Alternating Resistance Change. *Nanotechnology* **2017**, *28*, 355501.
(22) Hensel, A.; Schröter, C. J.; Schlicke, H.; Schulz, N.; Riekeberg, S.; Trieu, H. K.; Stierle, A.; Noei, H.; Weller, H.; Vossmeyer, T. Elasticity of Cross-Linked Titania Nanocrystal Assemblies Probed by AFM-Bulge Tests. *Nanomaterials* **2019**, *9*, 1230.
(23) Williams, G.; Seger, B.; Kamat, P. V. TiO_2-Graphene Nanocomposites. UV-Assisted Photocatalytic Reduction of Graphene Oxide. *ACS Nano* **2008**, *2*, 1487−1491.
(24) Panzarasa, G.; Soliveri, G. Photocatalytic Lithography. *Appl. Sci.* **2019**, *9*, 1266.
(25) Li, B.; Zhang, X.; Li, X.; Wang, L.; Han, R.; Liu, B.; Zheng, W.; Li, X.; Liu, Y. Photo-Assisted Preparation and Patterning of Large-Area Reduced Graphene Oxide−TiO_2 Conductive Thin Film. *Chem. Commun.* **2010**, *46*, 3499.
(26) Zhao, X.; Wang, Z.; Xie, Y.; Xu, H.; Zhu, J.; Zhang, X.; Liu, W.; Yang, G.; Ma, J.; Liu, Y. Photocatalytic Reduction of Graphene Oxide-TiO_2 Nanocomposites for Improving Resistive-Switching Memory Behaviors. *Small* **2018**, *14*, No. 1801325.
(27) Cai, X.; Ma, R.; Ozawa, T. C.; Sakai, N.; Funatsu, A.; Sasaki, T. Superlattice Assembly of Graphene Oxide (GO) and Titania Nanosheets: Fabrication, in Situ Photocatalytic Reduction of GO and Highly Improved Carrier Transport. *Nanoscale* **2014**, *6*, 14419−14427.
(28) Bell, N. J.; Ng, Y. H.; Du, A.; Coster, H.; Smith, S. C.; Amal, R. Understanding the Enhancement in Photoelectrochemical Properties of Photocatalytically Prepared TiO_2-Reduced Graphene Oxide Composite. *J. Phys. Chem. C* **2011**, *115*, 6004−6009.
(29) Lee, E.; Lee, D.; Yoon, J.; Yin, Y.; Lee, Y. N.; Uprety, S.; Yoon, Y. S.; Kim, D.-J. Enhanced Gas-Sensing Performance of GO/TiO_2 Composite by Photocatalysis. *Sensors* **2018**, *18*, 3334.

(30) Gordon, T. R.; Cargnello, M.; Paik, T.; Mangolini, F.; Weber, R. T.; Fornasiero, P.; Murray, C. B. Nonaqueous Synthesis of TiO_2 Nanocrystals Using TiF4 to Engineer Morphology, Oxygen Vacancy Concentration, and Photocatalytic Activity. *J. Am. Chem. Soc.* **2012**, *134*, 6751−6761.
(31) Chen, J.; Li, Y.; Huang, L.; Li, C.; Shi, G. High-Yield Preparation of Graphene Oxide from Small Graphite Flakes via an Improved Hummers Method with a Simple Purification Process. *Carbon* **2015**, *81*, 826−834.
(32) Sellschopp, K.; Heckel, W.; Gäding, J.; Schröter, C. J.; Hensel, A.; Vossmeyer, T.; Weller, H.; Müller, S.; Vonbun-Feldbauer, G. B. Shape-controlling effects of hydrohalic and carboxylic acids in TiO_2 nanoparticle synthesis. *J. Chem. Phys.* **2020**, *152*, No. 064702.
(33) Marcano, D. C.; Kosynkin, D. V.; Berlin, J. M.; Sinitskii, A.; Sun, Z.; Slesarev, A.; Alemany, L. B.; Lu, W.; Tour, J. M. Improved Synthesis of Graphene Oxide. *ACS Nano* **2010**, *4*, 4806−4814.
(34) Mills, A.; Lee, S.-K.; Lepre, A.; Parkin, I. P.; O'neill, S. A. Spectral and Photocatalytic Characteristics of TiO_2 CVD Films on Quartz. *Photochem. Photobiol. Sci.* **2002**, *1*, 865−868.
(35) Lerf, A.; He, H.; Forster, M.; Klinowski, J. Structure of Graphite Oxide Revisited. *J. Phys. Chem. B* **1998**, *102*, 4477−4482.
(36) Akhavan, O.; Ghaderi, E. Photocatalytic Reduction of Graphene Oxide Nanosheets on TiO_2 Thin Film for Photoinactivation of Bacteria in Solar Light Irradiation. *J. Phys. Chem. C* **2009**, *113*, 20214−20220.
(37) Pellegrin, Y.; Odobel, F. Sacrificial Electron Donor Reagents for Solar Fuel Production. *C. R. Chim.* **2017**, *20*, 283−295.
(38) Yang, H.; Amari, H.; Liu, L.; Zhao, C.; Gao, H.; He, A.; Browning, N. D.; Little, M. A.; Sprick, R. S.; Cooper, A. I. Nano-Assemblies of a Soluble Conjugated Organic Polymer and an Inorganic Semiconductor for Sacrificial Photocatalytic Hydrogen Production from Water. *Nanoscale* **2020**, *12*, 24488−24494.
(39) Akhavan, O.; Abdolahad, M.; Esfandiar, A.; Mohatashamifar, M. Photodegradation of Graphene Oxide Sheets by TiO_2 Nanoparticles after a Photocatalytic Reduction. *J. Phys. Chem. C* **2010**, *114*, 12955−12959.
(40) Radich, E. J.; Krenselewski, A. L.; Zhu, J.; Kamat, P. V. Is Graphene a Stable Platform for Photocatalysis? Mineralization of Reduced Graphene Oxide With UV-Irradiated TiO_2 Nanoparticles. *Chem. Mater.* **2014**, *26*, 4662−4668.
(41) Tian, J.; Zhao, Z.; Kumar, A.; Boughton, R. I.; Liu, H. Recent Progress in Design, Synthesis, and Applications of One-Dimensional TiO_2 Nanostructured Surface Heterostructures: A Review. *Chem. Soc. Rev.* **2014**, *43*, 6920−6937.
(42) Zhang, J.; Zhou, P.; Liu, J.; Yu, J. New Understanding of the Difference of Photocatalytic Activity among Anatase, Rutile and Brookite TiO_2. *Phys. Chem. Chem. Phys.* **2014**, *16*, 20382−20386.
(43) Kandiel, T. A.; Robben, L.; Alkaim, A.; Bahnemann, D. Brookite versus Anatase TiO_2 Photocatalysts: Phase Transformations and Photocatalytic Activities. *Photochem. Photobiol. Sci.* **2013**, *12*, 602−609.
(44) Li, Z.; Cong, S.; Xu, X. Brookite vs Anatase TiO_2 in the Photocatalytic Activity for Organic Degradation in Water. *ACS Catal.* **2014**, *4*, 3273−3280.
(45) Agmon, N. The Grotthuss Mechanism. *Chem. Phys. Lett.* **1995**, *244*, 456−462.
(46) Hatakeyama, K.; Karim, M. R.; Ogata, C.; Tateishi, H.; Funatsu, A.; Taniguchi, T.; Koinuma, M.; Hayami, S.; Matsumoto, Y. Proton Conductivities of Graphene Oxide Nanosheets: Single, Multilayer, and Modified Nanosheets. *Angew. Chem., Int. Ed.* **2014**, *53*, 6997−7000.
(47) He, P.; Brent, J. R.; Ding, H.; Yang, J.; Lewis, D. J.; O'brien, P.; Derby, B. Fully Printed High Performance Humidity Sensors Based on Two-Dimensional Materials. *Nanoscale* **2018**, *10*, 5599−5606.
(48) Guo, L.; Jiang, H.-B.; Shao, R.-Q.; Zhang, Y.-L.; Xie, S.-Y.; Wang, J.-N.; Li, X.-B.; Jiang, F.; Chen, Q.-D.; Zhang, T.; Sun, H.-B. Two-Beam-Laser Interference Mediated Reduction, Patterning and Nanostructuring of Graphene Oxide for the Production of a Flexible Humidity Sensing Device. *Carbon* **2012**, *50*, 1667−1673.
(49) Fatima, Q.; Haidry, A. A.; Yao, Z.; He, Y.; Li, Z.; Sun, L.; Xie, L. The Critical Role of Hydroxyl Groups in Water Vapor Sensing of Graphene Oxide. *Nanoscale Adv.* **2019**, *1*, 1319−1330.
(50) Mansour, E.; Vishinkin, R.; Rihet, S.; Saliba, W.; Fish, F.; Sarfati, P.; Haick, H. Measurement of Temperature and Relative Humidity in Exhaled Breath. *Sens. Actuator B: Chem.* **2020**, *304*, No. 127371.
(51) Singh, E.; Meyyappan, M.; Nalwa, H. S. Flexible Graphene-Based Wearable Gas and Chemical Sensors. *ACS Appl. Mater. Interfaces* **2017**, *9*, 34544−34586.
(52) Kulyk, B.; Silva, B. F. R.; Carvalho, A. F.; Barbosa, P.; Girão, A. V.; Deuermeier, J.; Fernandes, A. J. S.; Figueiredo, F. M. L.; Fortunato, E.; Costa, F. M. Laser-Induced Graphene from Paper by Ultraviolet Irradiation: Humidity and Temperature Sensors. *Adv. Mater. Technol.* **2022**, *7*, No. 2101311.
(53) Sauerbrey, G. Verwendung von Schwingquarzen zur Wägung dünner Schichten und zur Mikrowägung. *Z. Physik* **1959**, *155*, 206−222.
(54) Thommes, M.; Kaneko, K.; Neimark, A. V.; Olivier, J. P.; Rodriguez-reinoso, F.; Rouquerol, J.; Sing, K. S. Physisorption of Gases, with Special Reference to the Evaluation of Surface Area and Pore Size Distribution (IUPAC Technical Report). *Pure Appl. Chem.* **2015**, *87*, 1051−1069.

https://doi.org/10.1021/acsanm.4c06524
ACS Appl. Nano Mater. 2025, 8, 7428−7439